Mode I toughening of bio-based epoxy adhesive through 3D-printed biomimetic reinforcements

Tao, Ran; Xu, Zhiyuan; Teixeira de Freitas, Sofia

DOI
10.1016/j.compositesb.2025.113313

Publication date
2026

Document Version
Final published version

Published in
Composites Part B: Engineering

Citation (APA)
Tao, R., Xu, Z., & Teixeira de Freitas, S. (2026). Mode I toughening of bio-based epoxy adhesive through 3D-printed biomimetic reinforcements. *Composites Part B: Engineering*, *312*, Article 113313. https://doi.org/10.1016/j.compositesb.2025.113313

Composites Part B 312 (2026) 113313

Contents lists available at ScienceDirect

Composites Part B

journal homepage: www.elsevier.com/locate/composites

Mode I toughening of bio-based epoxy adhesive through 3D-printed biomimetic reinforcements

Ran Tao [a], Zhiyuan Xu [a], Sofia Teixeira de Freitas [a,b,*]

[a] *Aerospace Structures & Materials, Faculty of Aerospace Engineering, Delft University of Technology, The Netherlands*
[b] *IDMEC, Instituto Superior Técnico, University of Lisbon, Portugal*

ARTICLE INFO

Dataset link: 10.4121/51d38e1c-3266-4975-be96-97a658ffc186

Keywords:
Biomimetic
Bio-based epoxy
3D printing
Adhesive joint
Toughness

ABSTRACT

Bio-based epoxy adhesives face significant challenges due to their relatively poor mechanical properties compared to their petroleum-based competitors, including low fracture toughness and abrupt failure. By mimicking the molecular structure of spider silk, which is one of the toughest materials in nature, 3D-printed polymer overlapping curls consisting of coiling fibers with sacrificial bonds and hidden lengths, were impregnated into a bio-based epoxy adhesive to improve its mode I fracture toughness. Such bio-inspired structures were designed specifically to toughen and improve the crack resistance of adhesive joints. These overlapping curls were embedded in the bio-based epoxy bondline with various adhesion patterning strategies, aiming to architect the fracture scenario and increase mode I energy dissipation. Double cantilever beam test results show that an extrinsic bridging is triggered by the embedded curls that promote progressive failure and delay crack growth, which improved the mean energy release rate by 133% and enhanced the mean peak energy release rate up to 313%. The proposed 3D-printed coiling fibers successfully improved the mechanical performance of the bio-based epoxy and retarded the crack growth within the bondline, opening new horizons for their use as carriers of bondlines in structural applications to control crack growth in adhesively bonded joints.

1. Introduction

Climate change is a major global issue that impacts both the environment and human society, requiring an immediate effort to enhance sustainability in the mobility and energy sectors. Carbon fiber-reinforced polymers (CFRPs) have been widely applied in aerospace, automotive, marine, and sports industries, due to their high strength and light weight [1,2]. Using adhesive bonding in lightweight composite structures is a rising state-of-the-art technique that contributes to more efficient, sustainable, and lightweight load-bearing structures [3,4]. However, most conventional adhesive materials are petroleum-based epoxy resins, exacerbating the growing environmental, healthy, and economic concerns due to the harmful industrial processes and finite petrochemical resources. The green transition is essential for positioning bio-based adhesive materials as attracting options for integration into load-bearing structures. However, research shows that when replacing the petroleum-based components with bio-based components in the epoxy formulations, the mechanical properties decrease significantly, limiting their application in load-bearing structures [5,6]. To enhance sustainability and concurrently uphold joint safety and reliability, there is a need to improve the mechanical properties of bio-based epoxy adhesives.

Several methods have been investigated to improve the fracture resistance of (petroleum-based) adhesive joints that establish the current state-of-the-art on the topic. The introduction of crack arrest features, such as the corrugated substrate [7], z-pins [8], and co-cured thermoplastic barrier [9], provides representative examples. Another promising pathway is to architect the adhesive layer and rely on the crack path strategies that promote crack competition, crack deflection, crack branching, and crack bridging. One of these examples is to utilize the adhesive layer directly to bridge the separating CFRP parts, triggered by the patterning of distinct surface treatments [10], where the patterning can be the combination of peel-ply surfaces, sanded surface, laser-treated, or plasma-activated [11–13]. Another example recently explored is to integrate lightweight meshes within the adhesive layer that further improve the progressive failure of bonded joints. The polymer carrier within the adhesive film, originally aiming for maintaining the bondline thickness, has been proven to largely enhance the energy release rate (ERR) and successfully arrest the crack propagation [14]. Following this trend, polyamide structures (individual

---

[*] Corresponding author at: Aerospace Structures & Materials, Faculty of Aerospace Engineering, Delft University of Technology, The Netherlands.
E-mail address: s.teixeiradefreitas@tudelft.nl (S. Teixeira de Freitas).

https://doi.org/10.1016/j.compositesb.2025.113313
Received 3 October 2025; Received in revised form 19 November 2025; Accepted 10 December 2025

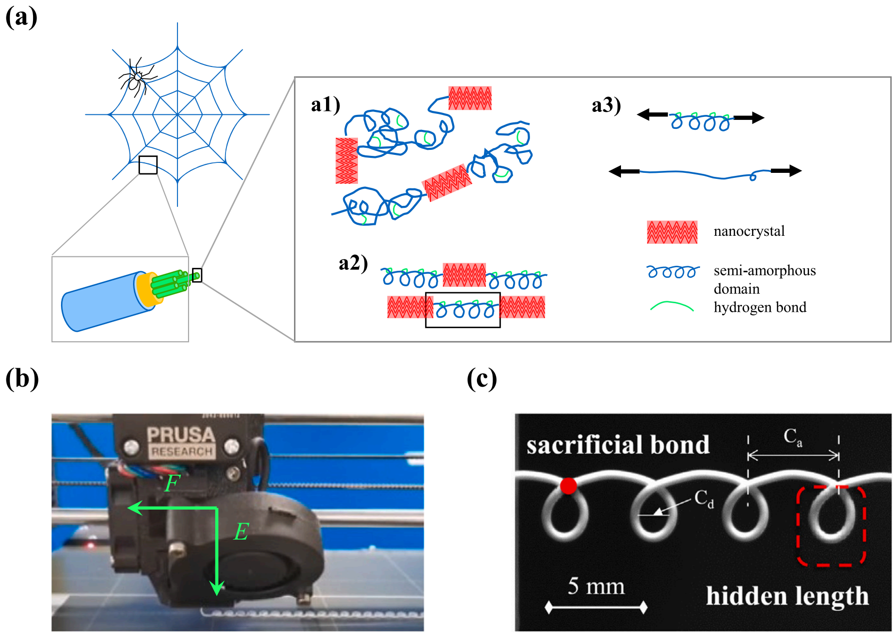

Fig. 1. (a) Overlapping curl structures bio-inspired by the spider silk [17,18]. (b) Manufacturing of OC through the liquid rope coiling of a 3D printer. F is the moving speed of printing nozzle, and E is the extrusion speed of melted polymer. (c) 3D-printed biomimetic OC structure, where the red dot highlights the sacrificial bonds and the dashed box indicates the curl contains hidden length. C_d is the diameter of the curl and C_a is the pitch distance between curls. (For interpretation of the references to color in this figure legend, the reader is referred to the web version of this article.)

straight wire [15] and woven 2D net [16]) were integrated into double cantilever beams (DCBs) to improve joint fracture resistance [15,16]. However, these embedded structures have been limited to simple topologies, such as 1D or a 2D network of straight wires. To take full advantage of the extrinsic bridging of these embedded structures and further enhance the crack delaying capability, the topology of these embedded carrier structures needs to be specifically architected for toughness improvement, rather than random topologies.

Through billions of years of evolution in their structure and architecture, natural materials often achieve high mechanical performance with low to none environmental impact, despite consisting of weak material components [19]. Spider silk is one of the interesting natural structure materials showing super tough properties, thanks to its hierarchical molecular architecture combining the nanocrystals and semi-amorphous domains, as schematic in Fig. 1(a) [17,20,21]. The hydrogen bonds within the semi-amorphous domains give serrated load responses (Fig. 1 a1)), which could simplify the silk structure as the schematic in Fig. 1 a2). The unravel of semi-amorphous domains (Fig. 1 a3)) provides a large extensibility, and the final loading on nanocrystals controls the ultimate strength. Such typical architecture is the key to the supreme strength and toughness of spider silk [20,21], which triggered several biomimetic studies to scale up and apply this promising structure. An example is a stretchable fiber, which adopted a core–shell structure to mimic the serrated load response, achieving a large stretchability with enhanced toughness [22]. However, the manufacturing of the core–shell structure is complex, and the failure responses highly depend on the material properties. A more promising strategy is to use the 3D printing technique to produce such an extensible structure in one step [23,24]. The effects of 3D printing parameters on structural failure responses were thoroughly investigated, and the serrated load behavior relies mainly on the topology. These 3D-printed tough structures were embedded in an elastomer and prove to enhance its impact resistance [17], showing a large-scale toughening of soft structures. However, up to now, no reported research has integrated this biomimetic structure as a mesh into adhesively bonded joints using bio-based epoxy adhesives.

In this work, we aim to toughen mode I fracture behavior of adhesively bonded joints through integrating the spider-silk biomimetic design within a bio-based epoxy adhesive. By mimicking the molecular structure of spider silk, polyamide (PA) coiling fibers with sacrificial bonds and hidden lengths were manufactured through 3D printing and embedded into a bio-based epoxy. Such 3D-printed biomimetic reinforcements, or overlapping curls (OCs), have the advantage of great extensibility and enhanced energy dissipation [24]. Different from previous work simply using the line wires or network [15,16], the biomimetic OC structure is designed specifically to toughen the mode I energy dissipation in a longer range and achieved higher energy release rate (ERR), since a larger displacement at failure of the bridging elements is expected to further arrest the crack propagation and improve ERR [25].

2. Materials and methods

2.1. Material

Bonding substrates were $[0]_8$ carbon fiber reinforced polymers (CFRPs), made through manual stacking of unidirectional prepregs (HexPly 8552/AS4, Hexcel, USA). The substrates were cured following the supplier's recommendation in the autoclave, which consisted of a 2 °C/min heating up to 110 °C, holding at 110 °C for 60 min, 2 °C/min heating to 180 °C, 120 min holding at 180 °C, and 2 °C/min cooling till 20 °C. Throughout the thermal cycle, the substrates were kept within the vacuum bag under an extra 7 bar pressure in the autoclave. Cured plates had a nominal thickness of 1.5 mm, and they were then cut into slices with dimensions of 200 mm × 25 mm for manufacturing double cantilever beam (DCB) samples. Biomimetic structures were 3D-printed out of polyamide 6 filament (F3 PA Pure Pro, FiberThree, Germany). To bond the cured CFRP substrates, GreenCast 160 bio-based epoxy resin (Sicomin, France) was adopted in this work for the adhesive material. GreenCast 160 was mixed with the hardener SD 7160 at a weight ratio of 100:42, and then the mixture was degassed under vacuum for 30 min before bonding.

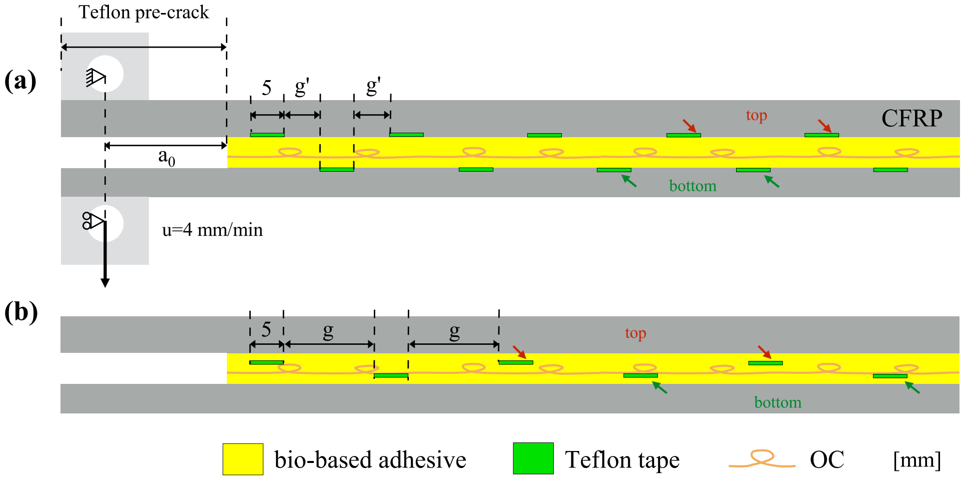

Fig. 2. Schematics of bondline configurations with various integrated OC structures. (a) Substrate adhesion patterning (**SP**), with constant gap distance $g' = 5$ mm. (b) OC adhesion patterning, with three gap distance values were adopted: **G5** ($g = 5$ mm), **G10** ($g = 10$ mm), and **G15** ($g = 15$ mm). (For interpretation of the references to color in this figure legend, the reader is referred to the web version of this article.)

Table 1
The printing parameters and obtained OC geometric details.

Printing diameters	Values	Mean OC geometry	Values, mm
Nozzle diamater	0.4 mm	OC filament diameter	0.55 ± 0.02
Nozzle temperature	275 °C	Curl diameter C_d	2.11 ± 0.18
Printing bed temperature	80 °C	Curl pitch C_a	3.19 ± 0.13
Nozzle height	5 mm	Curl hidden length	6.61 ± 0.08
Filament extrusion speed E	60 mm/min		
Nozzle moving speed F	1000 mm/min		

Table 2
Bondline configurations in DCB testing samples.

Configuration	Description	Gap distance, mm
Pure	Pure bio-based epoxy adhesive	–
SP	Substrate adhesion patterning on adherends	5
G5	OC adhesion patterning	5
G10	OC adhesion patterning	10
G15	OC adhesion patterning	15

2.2. Manufacture biomimetic structures

Biomimetic overlapping curls were 3D printed through honey-like liquid rope coiling by adjusting the extrusion and printing speed ratio of a fused filament fabrication printer (Prusa i3 MK3S+, Prusa Research, Czech Republic), as shown in Fig. 1(b). With manufacturing parameters chosen to have the optimized extension under the bondline thickness constraint [24], polyamide OC structures were obtained, consisting of coiling fibers with sacrificial bonds and hidden length. The specific parameters are summarized in Table 1. A close observation of the OC structure is highlighted in Fig. 1(c), where C_d is the diameter of the curl and C_a is the pitch distance between curls (Table 1).

2.3. Bondline architecting with biomimetic OC structures

Various bondline configurations were prepared to fully investigate the effect of the integrated biomimetic OC structures. The nominal bondline thickness (t_a) was kept constant at 1 mm in all configurations. The reference baseline condition **Pure** consists of pure bio-based epoxy adhesive layer, without any embedded reinforcement. To architect the crack path and promote OC bridging within DCB samples, two different adhesion patterning strategies were employed in the DCB bonded joints containing embedded OCs. On both cases, the adhesion was materialized by Teflon tapes (5 mm wide, 0.05 mm thick) alternatively patterned on top and bottom sides of the adhesive layer.

The first adhesion patterning is placed at the CFRP substrates, where the Teflon tapes were employed alternatively on the two substrate CFRP with a gap distance of $g' = 5$ mm (Fig. 2(a)), which is named as substrate patterning **SP** in this work. The manufacturing process of this substrate adhesion patterning can be viewed in Figs. 3(a) and (b). Such a substrate patterning aims to guide the crack path alternatively on two epoxy/CFRP interfaces, to trigger the bridging of adhesive ligaments and then the unfolding of the OCs [10,15].

The second adhesion patterning strategy is at the OCs themselves, where the Teflon tapes were positioned on opposite faces of OCs with a gap distance g — see Fig. 2(b). Three adhesion patterns were conceived, with constant gap distances g, **G5** is $g = 5$ mm, **G10** stands for $g = 10$ mm, and **G15** represents $g = 15$ mm. The manufacturing process of this OC adhesion patterning are shown in Fig. 3(a), where red arrows highlight the adhesion patterning on top surfaces of OCs and green arrows indicate the adhesion patterning on bottom OCs. Table 2 lists the five DCB configurations investigated in this work.

When preparing the bonding, a proper surface treatment was applied to the CFRP substrates to ensure good adhesion and cohesive failure during DCB tests. The surfaces were first sanded with a #400 sandpaper to create proper surface roughness. After being wiped with acetone, substrate surfaces were treated with UV/ozone for 7 min to activate the surface [26]. During adhesive bonding, the degassed adhesive mixture was first poured onto one of the CFRP surfaces. After placing the OCs on the liquid adhesive, the adhesive mixture was applied again to fully immerse OCs, as shown in Fig. 3(b). At last, the other CFRP substrate was gently pressed to the bondline under mechanical pressure, to ensure contact at CFRP/bondline interfaces. A pre-crack was generated through a 50 mm-long Teflon tape (0.05 mm thick) at the beginning of one of the CFRP surfaces, leading to a nominal initial crack length $a_0 = 35$ mm. The average actual crack length is 37 mm. One-mm spacers were placed at two ends to control the bondline thickness of DCB samples. The bonded DCB samples were cured under the room conditions (22 °C and 42% relative humidity) for 14 days before mode I tests.

2.4. Mechanical DCB tests

Quasi-static DCB tests were carried out to evaluate the mode I ERR of adhesive joints using a universal testing machine (Zwick 10 kN loading frame, ZwickRoell, Netherlands) with a 1 kN load cell, as illustrated in Fig. 3(c). Aluminum blocks were adhered to one end of

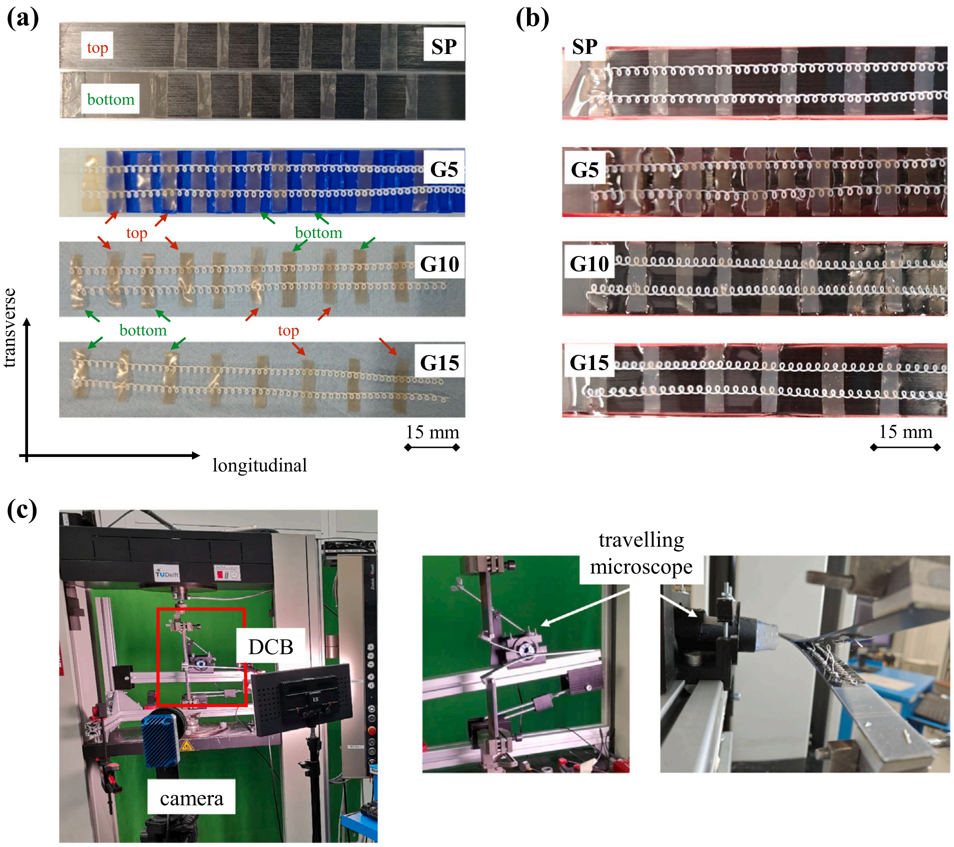

Fig. 3. (a) Top view of substrate adhesion patterning (**SP**) and OC adhesion patterning (**G5**, **G10**, and **G15**). (b) Top view of OCs integrated within the bio-based epoxy adhesive during bonding of DCB samples. (c) Set up of DCB testing. (For interpretation of the references to color in this figure legend, the reader is referred to the web version of this article.)

DCB samples, and metal pins were used for loading to ensure an aligned opening force. To highlight the crack advance, one side of the DCB samples was painted white, and a ruler was drawn manually with a resolution of 1 mm. DCB samples with pure bio-based epoxy bondline and OC-integrated bondline were tested, as described above and summarized in Table 2. For each bondline configuration, four samples were tested under 4 mm/min displacement control, and the loading conditions are schematically shown in Fig. 2(a). During the tests, the crack advance was recorded by a fixed camera from the ruler side of the DCB samples. In addition, a traveling microscope was mounted on the other side of the DCB samples, highlighted in Fig. 3(c), to closely visualize the crack morphology and fracture mechanisms. Both cameras captured images automatically every four seconds, synchronized with corresponding load and displacement data from the testing machine. Mode I ERR was obtained following the compliance calibration (CC) data reduction method, following ASTM D5528 standard [27], with an average calibration spacing of 4 mm.

3. Results and discussions

3.1. Substrate adhesion patterning

Typical DCB results of the baseline **Pure** and substrate patterning **SP** are shown in Fig. 4. Both **Pure** and **SP** demonstrate stick–slip load–displacement responses, while **SP** illustrates a larger fluctuation. With the surface adhesion patterning, **SP** improves average ERR from 0.30 ± 0.05 kJ/m^2 in **Pure** to 0.45 ± 0.14 kJ/m^2. On the baseline bio-based epoxy bondline **Pure** (Fig. 4(c)), cohesive failure is observed. While interfacial failure at both substrates is identified in **SP**, showing a crack path guided by the substrate patterning. With the presence of the adhesion patterning on the opposite substrate, a new crack is initiated and the crack path transits from the top to bottom substrate, triggering an adhesive ligament bridging [10,15], as highlighted in the in situ side observations in Fig. 4(d). However, due to the brittleness of the bio-based epoxy adhesive, the adhesive ligament breaks while generating the bridging, and on the way the OCs also break together with the adhesive ligament before any unfolding or bridging is triggered. Breakage of OCs at the edge of the **SP** patterning can be clearly shown in Fig. 4(d). As the crack propagates, the crack path deviates between two epoxy/CFRP interfaces, exposing integrated OCs and forming a large interfacial failure (Fig. 4(d)).

Therefore, although a 50% ERR enhancement could be achieved by **SP**, the substrate adhesion patterning strategy failed to promote the bridging of integrated OCs, mainly because of the sudden break of adhesive ligament bridging due to the brittle nature of the adopted bio-based epoxy adhesive material.

3.2. OC adhesion patterning

Typical DCB results of OC-integrated bondline with constant OC-patterning distance **G5**, **G10**, and **G15** are demonstrated in Fig. 5, with the comparison to baseline **Pure** and substrate patterning **SP**. For each bondline configuration, load–displacement curves, crack advancing, R-curves, and corresponding fracture surfaces after DCB testing are shown to highlight the crack propagation delay and energy dissipation enhancement due to the bondline architecting. The crack advancing plots, Figs. 5(a2), (b2), and (c2), highlight the crack propagation delays. Dashed lines are the linear fitting of crack length and extension data points, defining the crack delay coefficient with the comparison of fitted slope: $(\bar{c}_{OC} - \bar{c}_{Pure})/\bar{c}_{Pure} \times 100\%$, where $\bar{c}$ is the average value of four inverses of fitted slopes (k_i) in each bondline configuration

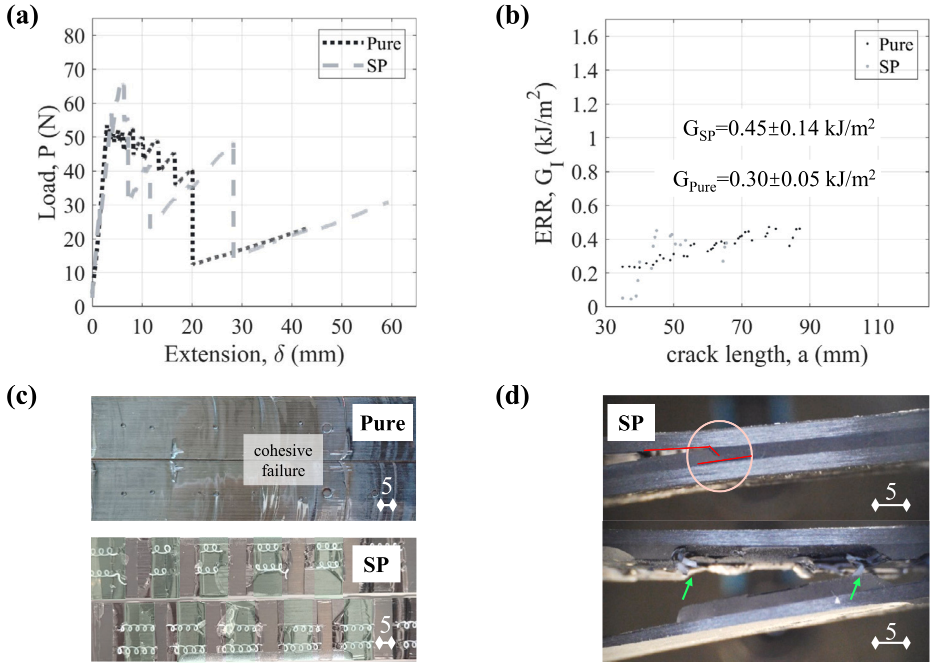

Fig. 4. (a) Load–displacement responses, (b) R-curves, and (c) fracture surfaces of **Pure** and **SP**. (d) In situ observation of **SP**. The scales in observations (c) and (d) are all 5 mm in length. The shaded regions highlight the interfacial failure locations in **SP** in (c), while the crack path is highlighted by the red lines and the broken OCs are highlighted by the green arrows in (d). (For interpretation of the references to color in this figure legend, the reader is referred to the web version of this article.)

$\bar{c} = \frac{\sum \frac{1}{k_i}}{4}$ and the subscript *OC* represents the bondline with integrated OCs and *Pure* stands for the baseline condition **Pure**. Such a crack delay coefficient represents quantitatively the crack delaying ability of the architected bondline compared to the baseline **Pure**.

The load–displacement curves of the DCB samples with constant OC adhesion patterning, **G5**, **G10**, and **G15**, show larger fluctuation amplitudes but lower variation frequency, comparing to the baseline **Pure** configurations. Compared to a relatively small crack delay of **SP** (crack delay coefficient is 38%), the crack delay of **G5** is largely increased (103%), and it reaches up to 136% in **G10**. The crack delaying is less significant when the gap distance further increases (**G15**), dropping to 124%. Corresponding to the stick–slip load–displacement curve, the R-curves of three configurations feature ERR peaks, evidence of multiple crack delay features during DCB tests. The fracture surfaces are aligned with the R-curves based on the crack length in Figs. 5(a3), (b3), and (c3), where the dashed lines are placed to better link the fracture surfaces and ERR variations. More detailed observations during the DCB tests are also included in the supplementary material (Fig. S1, Fig. S2, and Fig. S3). The enlarged fracture surfaces are also shown in the supplementary material (Fig. S4) for more detailed observations.

To better understand the role of the OC adhesion patterning, the correlation between ERR peaks and the OC adhesion patterning locations is highlighted by green dashed lines on the fracture surfaces in Fig. 5. ERR peaks in **G5** correlate well with the green dashed lines, illustrating the positive effects of the adhesion patterning on the crack delay and ERR enhancement. Most ERR peaks in **G10** demonstrate a similar failure scenario, while a few ERR peaks deviate from the OC adhesion patterning locations. Such deviation increases in **G15**.

It is therefore clear that the adhesion patterning has an important role in the increase of the ERR and crack delay. In the following subsections, the mechanisms behind this role will be further detailed.

3.2.1. Crack path guidance mechanism

The effects of the OC adhesion patterning (**G5**, **G10**, and **G15**) are schematically demonstrated in Fig. 6. Different from the substrate patterning **SP** in Fig. 4(d), the OC adhesion patterning showed predominantly cohesive failure. In a short gap distance of the adhesion patterning, **G5** in Fig. 6(a1), the crack path has a sharp deflection angle, guiding the crack to propagate across OCs and generating unfolding and bridging of OCs. Such a failure mechanism is sketched in Fig. 6(b1). As the gap distance increases, the crack path deflection decreases (Fig. 6(b2)), but it is still efficient to expose OCs in **G10**. However, less deflection angle in the crack path, as illustrated in Fig. 6(b2), loads the exposed OCs more in the transverse direction, leading to several early detached OCs in Fig. 6(a2). While in **G15**, the large gap distance brings the weak epoxy/PA adhesion and the adhesive brittleness in evidence, which leads to fast crack propagation — see Fig. 6(a3). Therefore, a shorter gap distance could guide the crack path better and result in more frequent crack path transitions.

3.2.2. Extrinsic OC bridging mechanism

The major influence of the OC adhesion patterning is to expose integrated biomimetic OC structures and trigger the extrinsic OC bridging failure mechanism under mode I loading. Three examples of triggered OC bridging in **G5**, **G10**, and **G15** are illustrated in Figs. 7(a), (b), and (c), respectively. More detailed illustrations of **G5**, **G10**, and **G15** can be found in the supplementary material Figs. S1, S2 and S3. As the OC adhesion patterning triggered OC bridging, the unfolded OCs extended the bridging length and held the separating CFRP arms over a long range.

The failure sequence of the OC bridging triggered by the OC adhesion patterning is summarized in the schematic Fig. 7(d). Initially, the impregnated OC is loaded transversely (Fig. 7(d1)), limiting the unfold of the OCs and, hence, the bridging effect [24]. However, thanks to the OC adhesion patterning, the crack path is guided to alternate between top and bottom OC surfaces, as indicated in Figs. 7(d2) and (d3), allowing the integrated OC to be loaded longitudinally and enabling the hidden length to unfold, as the epoxy ligaments break (Figs. 7(d4) and (d5)). The crack propagates across OCs and the OCs start to bridge the separating arms, as illustrated in Fig. 7(d5). Finally the hidden length of OC is released, and long-range extrinsic bridging is achieved (Fig. 7(d6)).

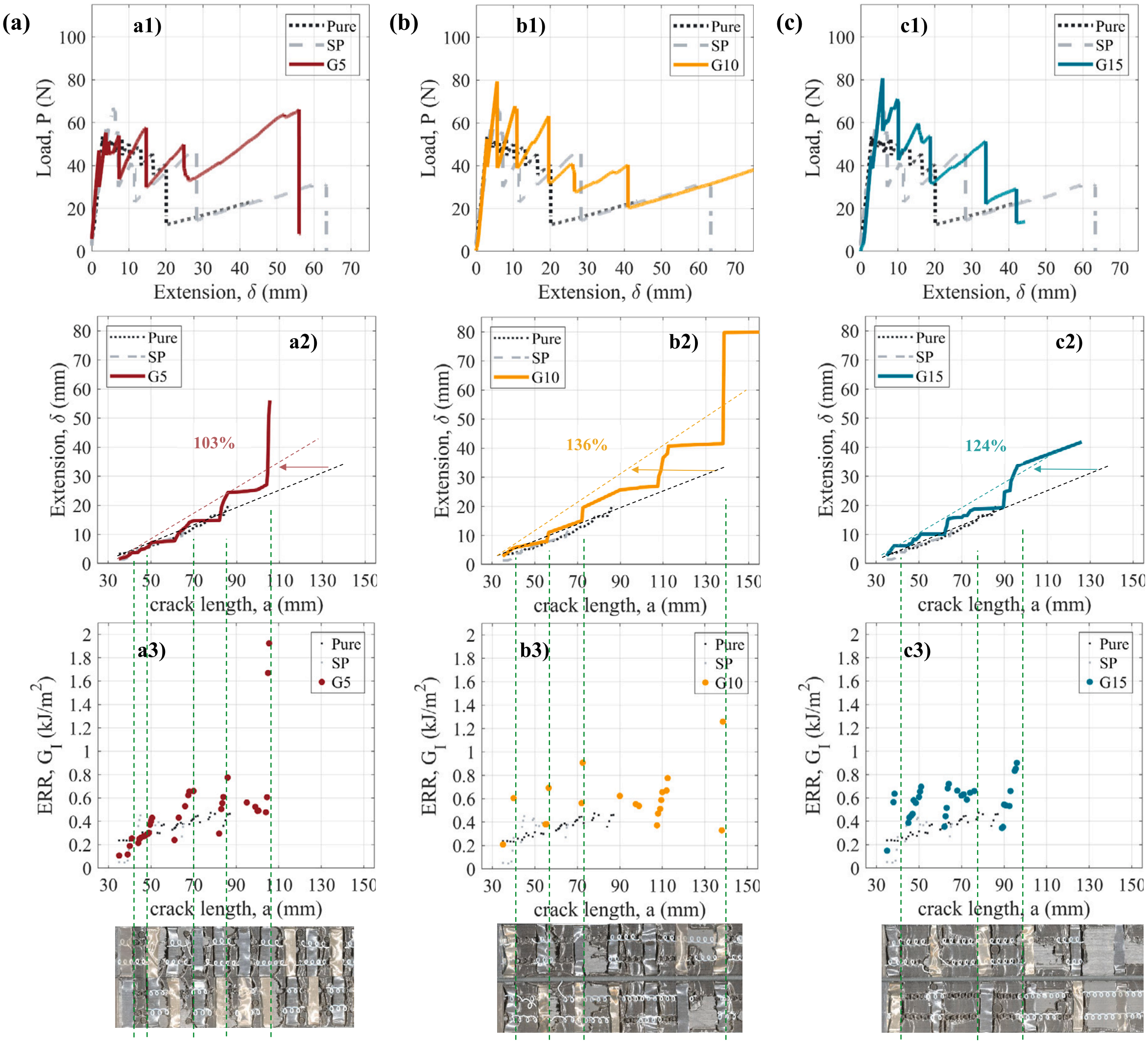

Fig. 5. Typical load–displacement curves, crack advancing, R-curves, and corresponding fracture surfaces of DCB samples with respect to the baseline **Pure** and **SP**, of three constant gap distances: (a) **G5**, (b) **G10**, and (c) **G15**. The arrows in crack advancing plots (a2), b2), and c2)) indicate the crack delay coefficients of each bondline configuration. The dashed lines in R-curves and corresponding fracture surfaces, a3), b3), and c3), highlight the adhesion patterning locations. The enlarged fracture surfaces are shown in the supplementary material Fig. S4. (For interpretation of the references to color in this figure legend, the reader is referred to the web version of this article.)

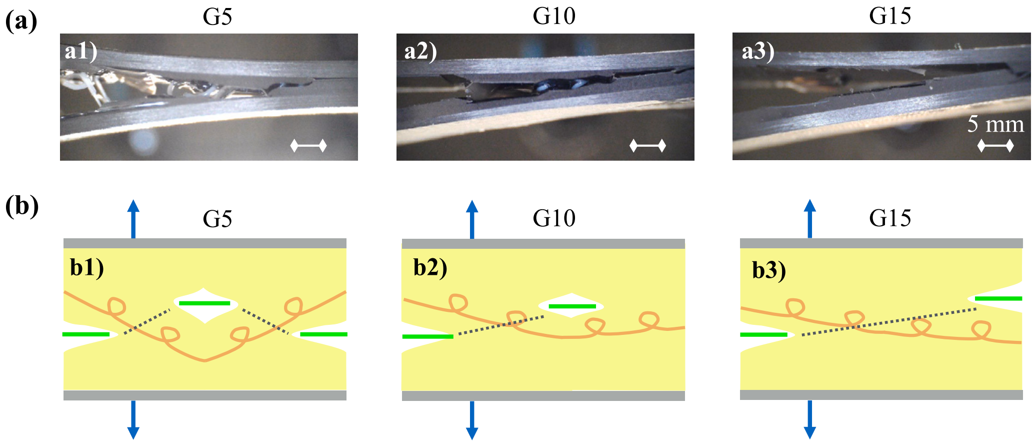

Fig. 6. In situ image observations of crack path morphology. (a) Adhesion patterning on OCs, (a1) **G5**, (a2) **G10**, and (a3) **G15**. (b) Schematics of the crack path control through the adhesion patterning, where green lines indicate the adhesion patterning and dashed lines indicate the potential crack path. (For interpretation of the references to color in this figure legend, the reader is referred to the web version of this article.)

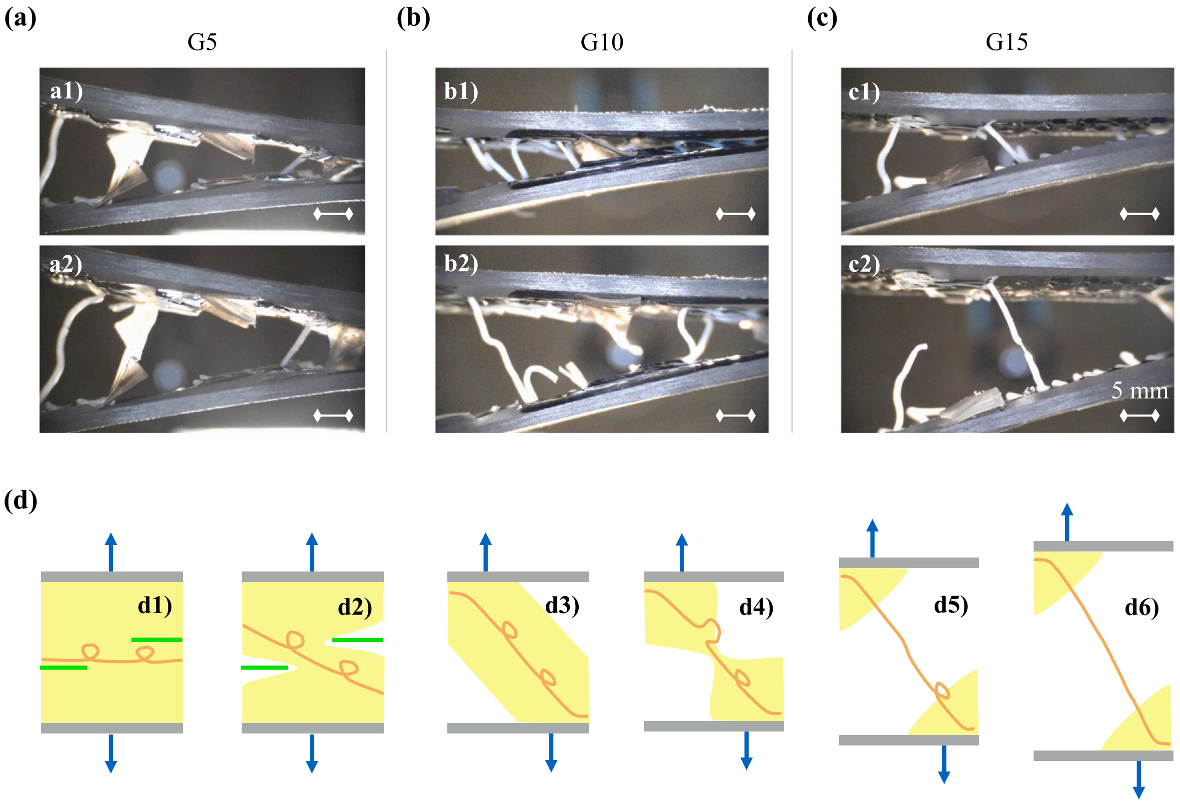

Fig. 7. In situ image observations of OC structure bridging of (a) **G5**, (b) **G10**, and (c) **G15**. (d) Schematics of the crack path control through the adhesion patterning, as indicated by the green lines. (For interpretation of the references to color in this figure legend, the reader is referred to the web version of this article.)

Unfortunately, such a failure procedure (shown in Fig. 7(d)) cannot be guaranteed for each DCB sample. As discussed in Fig. 6(c), the gap distance affected the crack path. The large gap distance often failed to guide the crack path across OCs and load OC longitudinally, resulting in less formation of the OC bridging. However, on the other hand, a large gap distance contains more hidden length in OC, potentially ending up with longer bridging OCs. These two side effects, of the number and length of the bridging, on the obtained mode I ERR values, as well as the large variations, are shown in ERR values of typical samples in Figs. 5(a3), (b3) and (c3), which requires a detailed comparison among three bondline configurations **G5**, **G10**, and **G15**.

3.3. Gap distance effects on mode I ERR

To better analyze the effect of the gap distance on ERR values within the configurations **G5**, **G10**, and **G15**, ERR values from all tested samples are summarized in Figs. 8(a), (b), and (c). Two types of average ERR values were determined. The first average ERR value is obtained when ERR is higher than 0.3 $\mathrm{kJ/m^2}$, referenced as the mean ERR of the configuration. The data points are highlighted by the large (light) shaded regions in Fig. 8, and the obtained average plateau ERR values are illustrated by the solid lines. While the second type of average ERR values is obtained considering the ERR peaks — defined as the local maximum of the ERR followed by a drop of more than 0.1 $\mathrm{kJ/m^2}$, viewed as the mean peak ERR of the configuration. The data points are highlighted by the small (dark) and sinuous shaded regions, and the obtained peak ERR values are illustrated as the dashed lines.

G5 demonstrates a more uniform distribution of peak values, while in bondline configurations **G10** and **G15**, two large peak ERR values greatly deviated from other ERR measurements, highlighted by the red arrows in Figs. 8(b) and (c). To better understand these peak ERR values, in situ observations and fracture surfaces at the largest peak ERR values of **G5**, **G10**, and **G15** are shown in Figs. 9(a), (b), and (c), respectively. On all fracture surface locations, highlighted by red arrows, cohesive failure transited to interfacial failure while obtained ERR values peaked in the range of 2.0 to 3.6 $\mathrm{kJ/m^2}$.

Through the in situ observations, **G5** has intensive OC bridging in both short and long sizes, indicating their positive contribution to the peak ERR value. While in **G10**, no clear OC bridging can be observed, but its ERR reaches the maximum of 3.6 $\mathrm{kJ/m^2}$. Therefore, it is clear that the largest peak ERR in **G10** does not stem from the OC bridging. The observation becomes more complex in **G15**, where only short OC bridging ($\approx$ 2 mm) is observed as the obtained ERR is 2.8 $\mathrm{kJ/m^2}$. Comparing to other peak ERR values of both **G10** and **G15**, where longer bridging OCs are observed in Figs. 7(b) and (c) and obtained ERR values are around 1.2 $\mathrm{kJ/m^2}$, the short OC bridging (Fig. 8(c)) could only contribute a small portion of the obtained peak ERR value.

The absence of large-scale OC bridging ($>$ 5 mm), in some peak ERR values of **G10** and **G15**, and transition from cohesive failure to interfacial failure implies that these peak ERR are not directly related with the OC bridging effect. The crack deflection and ERR peaks observed might still be related with the presence of the impregnated OCs coupled with the intrinsic fracture behavior of the bio-based epoxy adhesive. However, the understanding of such fracture phenomena are out of the scope of current work, as it is focused on the bridging effect of the OCs. Therefore, the following analyses of OC bridging effects are conducted after eliminating the peak ERR values without the presence of the large-scale OC bridging.

The updated ERR values from all DCB samples are demonstrated in Fig. 10, and updated mean ERR and mean peak ERR values are summarized in Table 3, where good correlations between peak ERR values and extrinsic OC bridging are guaranteed. The mean ERR represents more the overall dissipated energy of the bondline configuration, while the mean peak ERR is an indicator for the potential ultimate toughening of

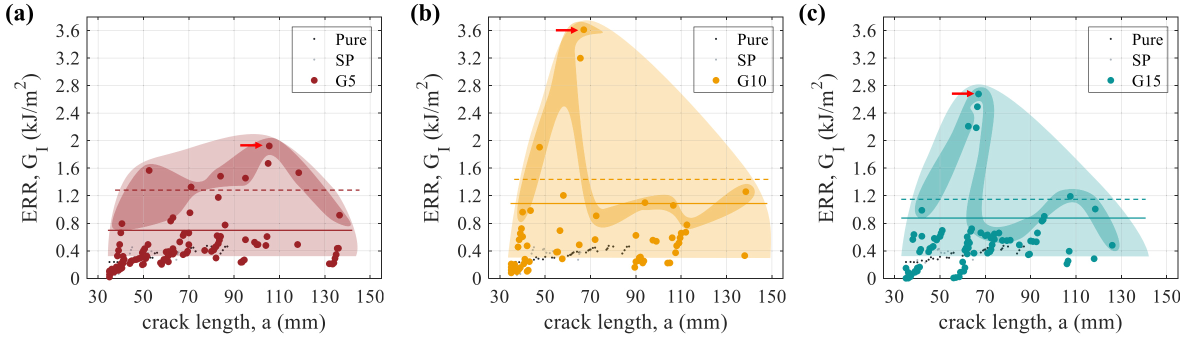

Fig. 8. Original ERR values from all DCB samples of (a) **G5**, (b) **G10**, and (c) **G15**. Large shaded regions highlight data points for mean ERR which are shown by the solid horizontal lines. Small shaded regions highlight data points for mean peak ERR that are shown by the dashed horizontal lines. Red arrows highlight the maximum peak ERR values. (For interpretation of the references to color in this figure legend, the reader is referred to the web version of this article.)

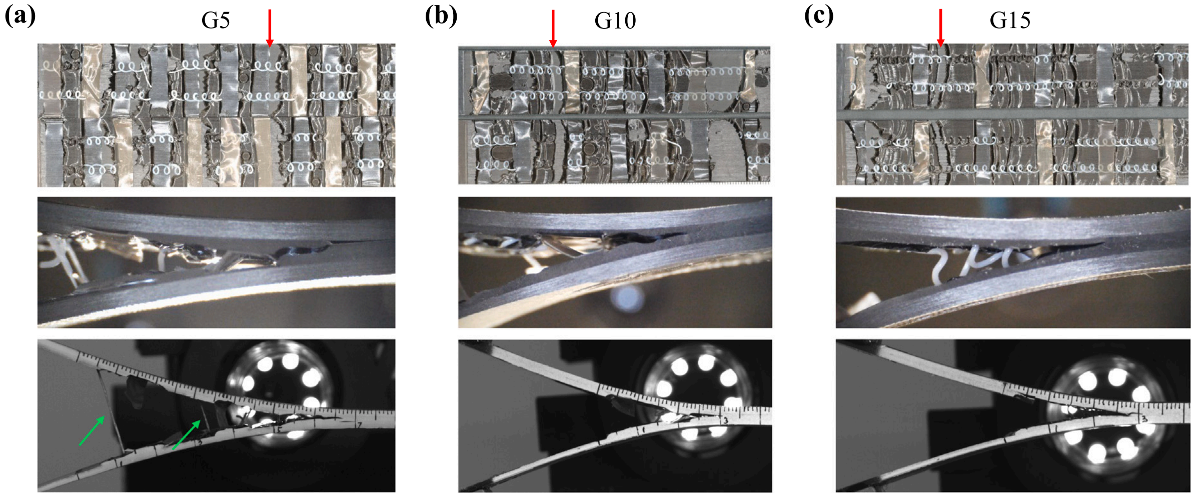

Fig. 9. In situ observations and fracture surfaces at two peak ERR values of (a) **G5**, (b) **G10**, and (c) **G15**. Vertical red arrows on the fracture surfaces highlight the locations of the in situ observations, and green arrows illustrate the large-scale OC bridging. (For interpretation of the references to color in this figure legend, the reader is referred to the web version of this article.)

the configuration when the crack path control is optimized. The mean ERR of the baseline **Pure** is averaged by all obtained ERR values, which is 0.30 kJ/m^2. The mean ERR of **SP** slightly increase to 0.45 kJ/m^2, which mainly came from the crack jump and adhesive ligament failure, as discussed in Fig. 4. Both mean ERR and mean peak ERR values are largely enhanced by the constant OC adhesion patterning **G5**, **G10**, and **G15**, where the **G5** configuration features an optimized toughening and achieves the highest both mean ERR and mean peak ERR values. Therefore, the OC adhesion patterning triggered more efficiently the OC bridging, compared to the substrate adhesion patterning **SP**, leading to higher ERR values and significant crack delaying in bondline configurations **G5**, **G10**, and **G15**.

G5 demonstrates a higher peak ERR than **G10**, indicating a more intensive OC bridging in smaller gap distance **G5**. As discussed in Figs. 6 and 7, the gap distance affects the crack path and potential OC bridging length. Higher ultimate ERR of **G5** proves that the crack path transition is more critical in toughening adhesive joints under the current material systems, where 5 mm of the gap distance enables more OC bridging. However, **G5** and **G10** are comparable in terms of the mean ERR. **G5** and **G10** increase the mean ERR by 133% than the baseline **Pure** bondline configuration. While when comparing the mean peak ERR, **G5** and **G10** increases the ERR by 313% and 247% in comparison with the baseline **Pure**, respectively. As the gap distance further increases to 15 mm, mean ERR and mean peak ERR leads to only 80% and 147% enhancement when compared to the baseline **Pure**, respectively. Both mean ERR and mean peak ERR values of **G15** are still larger than the substrate adhesion patterning **SP**, proving again a better toughening in the OC adhesion patterning strategy.

Table 3
Obtained ERR values averaged at the plateau and at the peaks, considering only peaks where toughening from the extrinsic bridging was visually observed, for constant gap distances of the adhesion patterning on OCs G5, G10, and G15. The original plateau and peak ERR values are calculated from the entire ERR values, while the plateau and peak ERR values are captured after eliminating the OC-interlocking-induced ERR values.

Configuration	Mean ERR, kJ/m^2	Mean peak ERR, kJ/m^2	Crack arresting, -
Pure	0.30 ± 0.05	–	–
SP	0.45 ± 0.14	0.50 ± 0.23	38%
G5	0.70 ± 0.18	1.24 ± 0.27	103%
G10	0.70 ± 0.17	1.04 ± 0.08	109%
G15	0.54 ± 0.03	0.74 ± 0.17	86%

The crack delaying, or crack delay coefficients, of three configurations are also compared in Table 3, where **G10** illustrates the largest crack arresting. Given the small differences in crack delay coefficient and large variations among samples, the crack delay of **G5** and **G10** are viewed as the same. Therefore, the trend of the crack arresting of three bondline configurations correlates well with the trend in their mean ERR. The short gap distance $g = 5$ mm in the OC adhesion patterning, **G5**, achieved the largest enhancement in mean peak mode I ERR. **G5** and **G10** both demonstrated over 100% crack delay and 133%

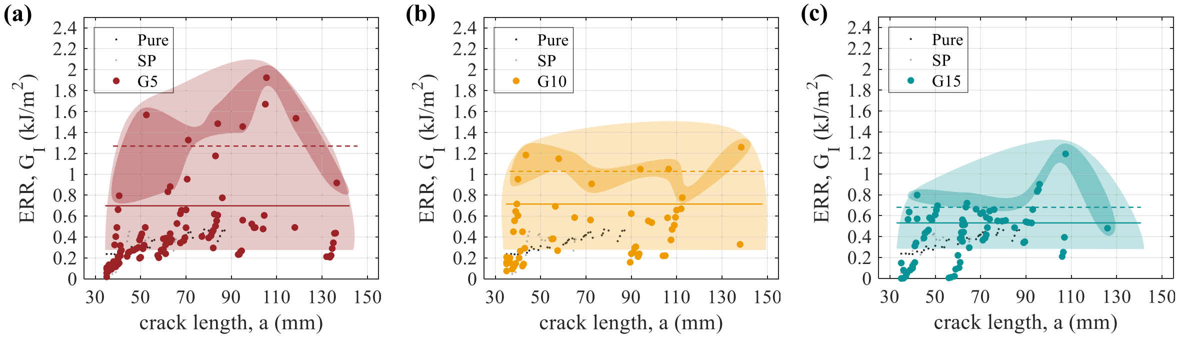

Fig. 10. ERR values, from all DCB samples of (a) **G5**, (b) **G10**, and (c) **G15**, with only toughening associated with the extrinsic bridging. Large shaded regions highlight data points for mean ERR which are shown by the solid horizontal lines. Small shaded regions highlight data points for mean peak ERR that are shown by the dashed horizontal lines.

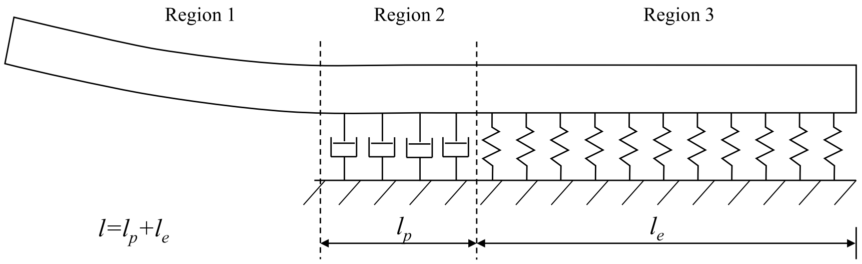

Fig. 11. Schematic of deformation zone within DCB samples under the elastic–plastic foundation theory [28,29].

larger mean ERR compared to the baseline **Pure** configuration. Such enhancement mainly came from the extrinsic bridging of biomimetic OC structures due to their specific topological design, instead of the increased energy dissipation within the adhesive [15].

In conclusion, the ability to delay the crack propagation has been greatly improved in the adhesively bonded composite structures, since the bridging OCs promote the progressive failure and largely delay the fast crack propagation. A short gap distance (e.g., g = 5 mm) is preferred in the current material system to achieve the most energy dissipation and the most crack delay feature. This fact can be partially related to the deformation zone length of this adhesive in the DCB configuration, as it will be discussed in the following section.

3.4. Deformation zone length

Mode I fracture onset can be investigated through the introduction of material and structural length scales [28]. Following S. E. Yamada's model [29], an elastic–plastic foundation model is adopted for the DCB sample, as illustrated in the schematic Fig. 11. The DCB sample is symmetric about the centerline of the adhesive layer, which is split into three regions. Region 1 is the free part of the DCB arm under the opening load. Region 2 is the part of the DCB arm supported by a perfectly plastic foundation (with a plastic process zone length l_p) due to the yielding of the adhesive material, depicted by damping elements. While region 3 is the part of the DCB arm supported by an elastic foundation, which has an elastic process zone length l_e and is indicated by spring elements.

The plastic process zone length is estimated by the fracture of the bulk adhesive material under the plane strain condition [30]:

$$l_p = \frac{1}{6\pi}\frac{E_a G_{Ia}}{\sigma_y^2}\frac{1}{(1-\nu_a^2)}, \tag{1}$$

where E_a is the adhesive Young's modulus, G_{Ia} is the mode I fracture toughness of the bulk adhesive, σ_y is the yield stress of the adhesive, and ν_a is the adhesive Poisson's ratio. While in region 3, the foundation stiffness k is [28]:

$$k = 2m_q\frac{E_a b}{t_a}, \tag{2}$$

where t_a is the adhesive bondline thickness, and under the plane strain condition m_q:

$$m_q = \frac{(1-\nu_a)}{(1-2\nu_a)(1+\nu_a)}. \tag{3}$$

In this way, the elastic process zone length is then defined as $l_e = \lambda^{-1}$, and λ is:

$$\lambda^4 = \frac{k}{4E_x^{sub}I}, \tag{4}$$

where $E_x^{sub}I$ is the bending stiffness of the DCB arm, $I = bh^3/12$ is the second moment of inertia of the DCB arm, and h is the thickness of the DCB arm. Then, substituting k and expanding I, λ can be rewritten in the following [28]:

$$\lambda^4 = 6m_q\frac{E_a}{E_x^{sub}}\frac{1}{t_a h^3}. \tag{5}$$

Based on the material characterization of the bio-based epoxy adhesive in our previous work [18], the Young's modulus of the bio-based epoxy is E_a = 667 MPa, and the yield stress of the bio-based epoxy is σ_y = 5.07 MPa. The Poisson's ratio is assumed to be ν_a = 0.3. The CFRP substrate has a longitudinal Young's modulus of E_x^{sub} = 141000 MPa [31] and a thickness of h = 1.5 mm. Taking the bondline thickness as t_a = 1 mm and the critical mode I fracture toughness of the bio-based epoxy G_{Ia} = 0.3 kJ/m^2, the plastic process zone can be estimated as l_p = 0.45 mm and the elastic process zone size l_e = 3.07 mm, giving a total deformation zone length of l = 3.52 mm.

The value of this deformation zone length is an underestimation calculation of the real value, since the critical mode I fracture toughness of a bulk bio-based epoxy is most likely larger than that in a confined condition, such as in a DCB [32]. Besides, the material properties of the bio-based epoxy E_a and σ_y might be slightly different due to a shorter curing time. To better show the consequences of bonding parameters,

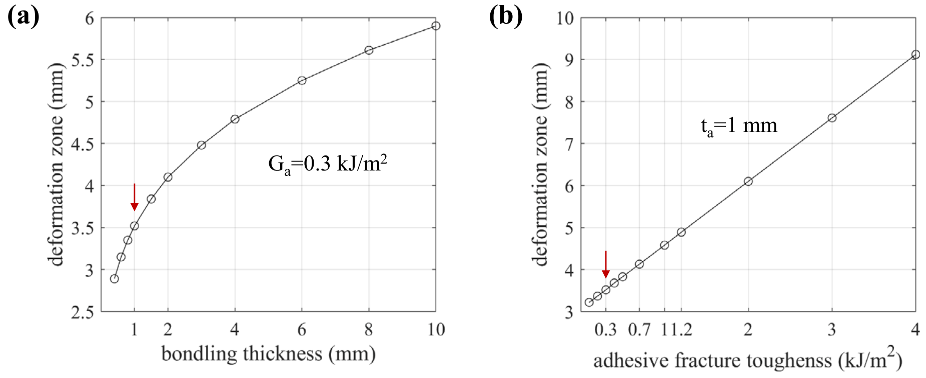

Fig. 12. Deformation zone length values varying versus (a) the bondline thickness t_a and (b) the adhesive bulk fracture toughness G_{Ia}. Red arrows highlight the data point of the experimental tests report before.

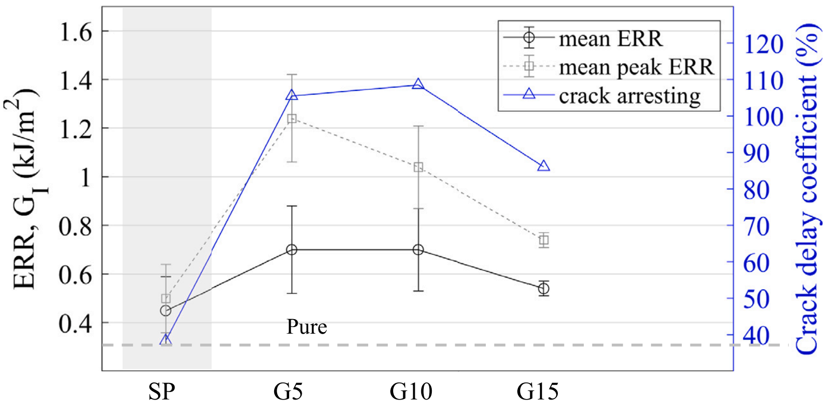

Fig. 13. Comparison plot for the average plateau and peak ERR values, as well as the crack delay coefficients.

variations of t_a and G_{Ia} were deployed, and the results are summarized in Fig. 12. The arrows point out the process zone lengths at $t_a = 1$ mm and $G_{Ia} = 0.3$ kJ/m^2. As a bold increase of t_a and G_{Ia}, the deformation zone length l only has limited increase from $l = 3.5$ mm up to $l = 10.0$ mm (at $t_a = 3$ mm and $G_{Ia} = 4.0$ kJ/m^2). This parametric sweep gives an indication of the possible range of deformation zone length l.

Comparing the value of the deformation zone length with the results of different OC patterning gap distances, it can be observed that when the gap distance is close to the deformation zone length $g \approx l$, it is easier to guide the crack path through the OC adhesion patterning. As the gap distance increases, e.g., $g = 15$ mm, the OC adhesion patterning fails to guide the crack propagation across OCs and the formation of extrinsic OC bridging is limited, leading to a decrease in ERR enhancement. This correlates well with the fact that $g = 15 \gg l = 10$ even under extreme bonding parameters (at $t_a = 3$ mm and $G_{Ia} = 4.0$ kJ/m^2). With the design space exploration shown in Fig. 12, a gap distance $g \in [3, 8]$ mm indicates a better toughening under the current material system.

This is of course a simplified analysis of the actual process zone length, but it already provides insights into the gap distance designs and the reasons behind the efficiency of the different gap distances. A deeper analysis with variation of adhesive thickness and corresponding gap distance could offer additional details on how impregnated OCs alters the deformation zone length, which could be one future research direction.

A visual comparison of various bondline configurations is demonstrated in Fig. 13. The baseline **Pure** is depicted as a dashed line in the plot, and the shaded region illustrates the substrate adhesion patterning **SP**. With the OC adhesion patterning within the bio-based epoxy bondline, compared to **SP**, both mean ERR and mean peak ERR of adhesive joints were enhanced, emphasizing the success of this adhesion patterning strategy. With extrinsic OC bridging, which adopts biomimetic designs consisting of sacrificial bonds and hidden length, **G5** and **G10** both show the maximum improvement (133%) than the baseline in mean ERR, while **G5** is able to enhance the mean peak ERR up to 313% when the OC bridging is fully activated. Correlating well with the deformation zone length estimation, short gap distance (**G5**) is more efficient to guide the crack path and delay the crack propagation through successfully triggered extrinsic OC bridging.

4. Conclusions

This work investigates the toughening effect of biomimetic overlapping curls, consisting of coiling fibers with sacrificial bonds and hidden length, in mode I fracture of adhesively bonded CFRP joints using the bio-based epoxy adhesive material. Biomimetic reinforcement coiling fibers were 3D printed, then adhesion patterned, and finally integrated within the bio-based epoxy adhesive. Five types of bondline configurations were architected, and they were tested through mode I DCB testing. Several conclusions can be drawn based on the current work:

- Using substrate adhesion patterning on CFRP, **SP**, mode I ERR has been increased by 50% when compared to the baseline **Pure** configuration, however the brittle nature of the adopted bio-based epoxy adhesive led to catastrophic failure and fast crack propagation;
- The OC adhesion patterning is crucial to efficiently trigger the OC bridging and arrest the crack propagation.
- Adhesion patterning with the gap distance of $g = 5$ mm gives the highest average ultimate ERR value;
- Compared to the baseline bio-based epoxy adhesive **Pure**, **G5** achieves up to 133% enhancement in the mode I mean ERR and 313% improvement in mean peak ERR;

- The adhesive's deformation zone length l, consisting of the elastic zone length and plastic zone length, ahead of the crack tip on the DCB seems to indicate an efficient gap distance: a $g \approx l$, which could be a design parameter for the OC adhesion patterning to guide the crack path and trigger more efficiently the OC bridging.

Therefore, integrated OC structures within the bio-based epoxy adhesive demonstrate a great potential in toughening strategy to delay the crack propagation and enhance mode I energy dissipation. Such a toughening strategy successfully brings ductility to the adhesive joints, and it is not limited to the bio-based epoxy. Furthermore, optimizing the adhesive material properties and their interactions with OCs opens more design potential for the toughened adhesive joints. However, the fracture responses still showed stick–slip behavior, which is the main limitation of the current work.

CRediT authorship contribution statement

Ran Tao: Writing – original draft, Methodology, Formal analysis, Data curation, Conceptualization. **Zhiyuan Xu:** Writing – review & editing, Methodology, Formal analysis, Data curation, Conceptualization. **Sofia Teixeira de Freitas:** Writing – review & editing, Supervision, Methodology, Funding acquisition, Formal analysis, Conceptualization.

Declaration of Generative AI and AI-assisted technologies in the writing process

The authors declare that no AI or AI-assisted technologies are involved in the writing process.

Declaration of competing interest

The authors declare the following financial interests/personal relationships which may be considered as potential competing interests: Sofia Teixeira de Freitas reports financial support was provided by Foundation for Science and Technology. If there are other authors, they declare that they have no known competing financial interests or personal relationships that could have appeared to influence the work reported in this paper.

Acknowledgment

The authors acknowledge Fundaca̧õ para a Cien̂cia e a Tecnologia (FCT) for its financial support via LAETA (project https://doi.org/10.54499/UID/50022/2025).

Appendix A. Supplementary data

Supplementary material related to this article can be found online at https://doi.org/10.1016/j.compositesb.2025.113313.

Data availability

The datasets obtained and/or analyzed during the current study are available on the 4TU DOI: 10.4121/51d38e1c-3266-4975-be96-97a658ffc186.

References

[1] Yildirim C, Ulus H, Sas HS, Yildiz M. Evaluating the influence of service conditions on the out-of-plane and in-plane loading performance and damage behavior of unidirectional CF/PEKK composites for aerospace applications. Compos Part B: Eng 2025;304:112637.
[2] Senol H, Ulus H, Al-Nadhari A, Topal S, Yildiz M. Ameliorating tensile and fracture performance of carbon fiber-epoxy composites via atmospheric plasma activation: Insights into damage modes through in-situ acoustic emission inspection. Compos Part A: Appl Sci Manuf 2025;195:108929.
[3] Schmid Fuertes TA, Kruse T, Körwien T, Geistbeck M. Bonding of CFRP primary aerospace structures, a discussion of the certification boundary conditions and related technology fields addressing the needs for development. Compos Interfaces 2015;22(8):795–808.
[4] Galvez P, Quesada A, Martinez MA, Abenojar J, Boada MJL, Diaz V. Study of the behaviour of adhesive joints of steel with CFRP for its application in bus structures. Compos Part B: Eng 2017;129:41–6.
[5] Saleh MN, Tomic NZ, Marinkovic A, Teixeira de Freitas S. The effect of modified tannic acid (TA) eco-epoxy adhesives on mode I fracture toughness of bonded joints. Polym Test 2021;96:107122.
[6] Tomic NZ, Saleh MN, Teixeira de Freitas S, Zivkovic A, Vuksanovic M, Poulis JA, et al. Enhanced interface adhesion by novel eco-epoxy adhesives based on the modified tannic acid on Al and CFRP adherends. Polymers 2020;12:1541.
[7] Tserpes KI, Peikert G, Floros IS. Crack stopping in composite adhesively bonded joints through corrugation. Theor Appl Fract Mech 2016;83:152–7.
[8] Hoffmann J, Scharr G. Mode I delamination fatigue resistance of unidirectional and quasi-isotropic composite laminates reinforced with rectangular z-pins. Compos Part A: Appl Sci Manuf 2018;115:228–35.
[9] Löbel T, Holzhüter D, Sinapius M, Hühne C. A hybrid bondline concept for bonded composite joints. Int J Adhes Adhes 2016;68:229–38.
[10] Tao R, Li X, Yudhanto A, Alfano M, Lubineau G. Laser-based interfacial patterning enables toughening of CFRP/epoxy joints through bridging of adhesive ligaments. Compos Part A: Appl Sci Manuf 2020;139(September):106094.
[11] Tao R, Alfano M, Lubineau G. Laser-based surface patterning of composite plates for improved secondary adhesive bonding. Compos Part A: Appl Sci Manuf 2018;109:84–94.
[12] Yildirim C, Ulus H, Beylergil B, Al-Nadhari A, Topal S, Yildiz M. Tailoring adherend surfaces for enhanced bonding in CF/PEKK composites: Comparative analysis of atmospheric plasma activation and conventional treatments. Compos Part A: Appl Sci Manuf 2024;180:108101.
[13] Senol H, Ulus H, Yildirim C, Al-Nadhari A, Topal S, Yildiz M. Assessing fracture toughness performance of adhesively bonded carbon fiber/epoxy composite joints accompanied by acoustic emission inspection: Effect of surface treatment methods. Eng Fract Mech 2025;321:111119.
[14] Heide-jørgensen S, Freitas D, Budzik MK. On the fracture behaviour of CFRP bonded joints under mode I loading: Effect of supporting carrier and interface contamination. Compos Sci Technol 2018;160:97–110.
[15] Tao R, Li X, Yudhanto A, Alfano M, Lubineau G. Toughening adhesive joints through crack path engineering using integrated polyamide wires. Compos Part A: Appl Sci Manuf 2022;158(January):106954.
[16] Yudhanto A, Almulhim M, Kamal F, Tao R, Fatta L, Alfano M, et al. Enhancement of fracture toughness in secondary bonded CFRP using hybrid thermoplastic/thermoset bondline architecture. Compos Sci Technol 2020;199(May):108346.
[17] Zou S, Therriault D, Gosselin FP. Spiderweb-inspired, transparent, impact-absorbing composite. Cell Rep Phys Sci 2020;1(11):100240.
[18] Xu Z, Tao R, Masania K, Teixeira de Freitas S. Bio-inspired overlapping curl structures for toughening bio-based epoxy: A study on the fracture phenomena. Compos Sci Technol 2025;272:111374.
[19] Wegst UGK, Bai H, Saiz E, Tomsia AP, Ritchie RO. Bioinspired structural materials. Nat Mater 2015;14(1):23–36.
[20] Nova A, Keten S, Pugno N, Redaelli A, Buehler M. Molecular and nanostructural mechanisms of deformation, strength and toughness of spider silk fibrils. Nat Preced 2010;1.
[21] Olive R, Cohen N. Deformation and failure mechanisms in spider silk fibers. J Mech Phys Solids 2024;182:105480.
[22] Cooper CB, Joshipura ID, Parekh DP, Norkett J, Mailen R, Miller VM, et al. Toughening stretchable fibers via serial fracturing of a metallic core. Sci Adv 2019;5(2):eaat4600.
[23] Passieux R, Guthrie L, Rad SH, Lévesque M, Therriault D, Gosselin FP. Instability-assisted direct writing of microstructured fibers featuring sacrificial bonds. Adv Mater 2015;27(24):3676–80.
[24] Xu Z, Tao R, Masania K, de Freitas ST. Biomimetic toughening design of 3D-printed polymeric structures: Enhancing toughness through sacrificial bonds and hidden lengths. Mater Des 2024;247:113361.
[25] Pulungan D, Andika S, Dirgantara T, Wirawan R, Judawisastra H, Wicaksono S. Promoting bridging in adhesively bonded composites with polymer inserts: A computational perspective. Compos Part A 2024;180:108107.

[26] Teixeira de Freitas S, Zarouchas D, Poulis JA. The use of acoustic emission and composite peel tests to detect weak adhesion in composite structures. J Adhes 2018;94(9):743–66.

[27] Standard test method for mode I interlaminar fracture toughness of unidirectional fiber-reinforced polymer matrix composites. ASTM Internat.; 2013.

[28] Fernandes RL, Budzik MK, Benedictus R, Teixeira de Freitas S. Multi-material adhesive joints with thick bond-lines: Crack onset and crack deflection. Compos Struct 2021;266:113687.

[29] Yamada SE. Elastic/plastic fracture analysis for bonded joints. Eng Fract Mech 1987;27(3):315–28.

[30] Kin Loch AJ, Shaw SJ. The fracture resistance of a toughened epoxy adhesive. J Adhes 1981;12(1):59–77.

[31] Lima RAA, Tao R, Bernasconi A, Carboni M, Carrere N, Teixeira De Freitas S. Uncovering the toughening mechanisms of bonded joints through tailored CFRP layup. Compos Part B: Eng 2023;263:110853.

[32] Fernandes LR, Teixeira De Freitas S, Budzik MK, Poulis JA, Benedictus R. From thin to extra-thick adhesive layer thicknesses: Fracture of bonded joints under mode I loading conditions. Eng Fract Mech 2019;218:106607.